ADVANCED ENERGY MATERIALS
www.advenergymat.de

Organic-Free and Lead-Free Perovskite Solar Cells with Efficiency over 11%

Weihai Zhang, Yating Cai, Heng Liu, Yu Xia, Jieshun Cui, Yueqing Shi, Rui Chen, Tingting Shi, and Hsing-Lin Wang**

Organic-free and lead-free $CsSnI_3$ perovskite solar cells (PSCs) have recently gained growing attention as a promising template to mitigate the thermal instability and lead toxicity of hybrid lead-based PSCs. However, the relatively low device efficiency due to the high content of Sn(II)-related defects hinders its further development. Herein, highly performed $CsSnI_{3-x}Br_x$ compositional perovskite-based PSCs are achieved by using dimethyl ketoxime (C_3H_7NO, DMKO) as a multifunctional additive. As a commercially used deoxidant, DMKO can effectively neutralize the oxygen molecule and reduce Sn^{4+} back to Sn^{2+}, enhancing the oxidation resistance of the film. Besides, the electron-rich oxime group (=NOH) in DMKO tends to interact with Sn^{2+} ions with extremely low adsorption energy less than −15 eV and inhibits defect formation, resulting in films with low defect density. The corresponding PSCs deliver a considerable open-circuit voltage (V_{oc}) of 0.75 V with a record efficiency as high as 11.2%, which represents the highest reported efficiency for lead-free all-inorganic PSCs thus far. More importantly, the grain surface distributed DMKO provides an in situ encapsulation of the perovskite, which results in greatly enhanced ambient stability of the un-encapsulated devices.

1. Introduction

Perovskite solar cells (PSCs) have achieved an exciting certified power conversion efficiency (PCE) of 25.7%, which is much higher than that of commercial multicrystalline silicon-based photovoltaic devices (23.3%), showing great potential toward practical applications.[1] However, thermal instability of organic components (e.g., methylammonium (MA) and formamidinium (FA)) and high toxicity of heavy metal lead (Pb) pose challenges for practical applications.[2–5] To address these issues, a new perovskite family of organic-free and lead-free cesium tin tri-iodide ($CsSnI_3$) has been proposed and attracted considerable attention.[6–8]

One of the potential candidates within the new perovskite family is the inorganic $CsSnI_3$. This kind of perovskite possesses favorable direct bandgap (around 1.3 eV), high optical absorption coefficient (about 10^4 cm^{-1} in the visible range), and ultralow exciton binding energy (18 meV), making it very promising as a photoactive layer for PSCs' construction.[9–11] Since the first report in 2014 by Kumar et al., the efficiency of $CsSnI_3$-based perovskite solar cells has witnessed steady improvement from 2.02% to 10.1% in 2021.[12,13] Such development has mainly been attributed to addressing the factors that affect the performance of the devices, such as annealing temperature,[14] film fabrication method,[15] and interface regulation.[16,17] However, little efforts have been made to

W. Zhang, H. Liu, Y. Xia, J. Cui, H.-L. Wang
Key University Laboratory of Highly Efficient Utilization of Solar Energy and Sustainable Development of Guangdong
Department of Materials Science and Engineering
Southern University of Science and Technology
Shenzhen 518055, China
E-mail: wangxl3@sustech.edu.cn

Y. Cai, T. Shi
Siyuan Laboratory
Guangzhou Key Laboratory of Vacuum Coating Technologies and New Energy Materials
Guangdong Provincial Engineering Technology Research Center of Vacuum Coating Technologies and New Energy Materials
Department of Physics
Jinan University
Guangzhou 510632, China
E-mail: ttshi@jnu.edu.cn

Y. Xia
School of Physics and Astronomy
University of Birmingham
Edgbaston, Birmingham B15 2TT, UK

Y. Shi, R. Chen
Department of Electrical and Electronic Engineering
Southern University of Science and Technology
Shenzhen 518055, China

The ORCID identification number(s) for the author(s) of this article can be found under https://doi.org/10.1002/aenm.202202491.

DOI: 10.1002/aenm.202202491

explore the effect of halide composition on the performance of $CsSnI_3$ perovskite-based devices. It is well known that the photovoltaic performance and stability of inorganic lead-based $CsPbI_{3-x}Br_x$ perovskite devices are largely depended on the I/Br ratio.[18–20] In this case, as a tin-based counterpart, it is necessary and imperative to conduct a systematic halide composition engineering study on $CsSnI_{3-x}Br_x$ perovskites to figure out the optimal I/Br ratio for efficient and stable tin-based inorganic PSCs.

Besides, it has been reported that Sn(II) induced defects, including heavily self-doping of Sn^{2+} to Sn^{4+}, tin-rich environment-induced Sn(I) antisite defects (Sn_I), and iodide vacancies (V_I), represent formidable factors for the huge open-circuit voltage loss ($V_{oc,loss}$) and poor device performance of tin-based PSCs.[21,22] Therefore, effective strategies that mitigate Sn(II)-induced defects are essential for high-performance devices. Previous studies have demonstrated that appropriate functional additive can effectively suppress Sn^{2+} oxidation. For instance, Yan and co-workers showed that antioxidant additive, such as hydroxybenzene sulfonic acid or its salt, can effectively suppress Sn^{2+} ions' oxidation.[23] The resulting $FASnI_3$-based device yields a PCE of 6.76% with enhanced air stability. Similarly, Priya and co-workers reported that the lone electron pairs of NH and CO units of *N,N*-methylenebis(acrylamide) (MBAA) can enhance the electron density around Sn^{2+} within the $CsSnI_3$ and protect it from oxidation to Sn^{4+}, delivering ambient stable device with a PCE of 7.5%.[24] Shortly after that, with localized electron density engineering, they further push the efficiency of $CsSnI_3$-based device to a record of 10.1% by using phthalimide (PTM) as an additive.[13] Since these results have demonstrated that an additive strategy is effective to improve the performance of tin-based PSCs by suppressing Sn^{2+} oxidation, appropriate additive candidate is expected to be more versatile. For example, a well-designed additive that can simultaneously mitigate Sn^{2+} oxidation and inhibit Sn_I and V_I defects' formation is believed to be able to reduce $V_{oc,loss}$, and further advance device performance.

Herein, we successfully fabricated a series of $CsSnI_{3-x}Br_x$-based PSCs by finely tuning the content of Br (x value). It demonstrates that the I/Br ratio can impact perovskite films' optical bandgap, and thus device performance. With an optimal x value at 0.4, the resulting devices produce a champion PCE of 9.19%. Further, we report simultaneous enhancement on the efficiency and stability of lead-free inorganic PSCs using dimethyl ketoxime (C_3H_7NO, abbreviated as DMKO) as an additive during film fabrication. On the one hand, as a commonly used deoxidant, DMKO can effectively neutralize the oxygen molecule and suppress Sn^{2+} oxidation, mitigating notorious self-doping of Sn^{2+} to Sn^{4+}. On the other hand, the electron-rich oxime group (=NOH) in DMKO can easily interact with Sn^{2+} ions and inhibit Sn_I and V_I formation. With this multifunctional additive, the resulting perovskite films show enhanced crystallinity with more uniform surface morphology, leading to long carrier lifetime, low defect density, and high electron mobility. Consequently, with optimal DMKO addition, the as-fabricated devices based on $CsSnI_{2.6}Br_{0.4}$ perovskite yield a record PCE of 11.2%, together with much-improved long-term, thermal as well as ambient stability.

2. Results and Discussion

Lead-free inorganic $CsSnI_{3-x}Br_x$ perovskite films were fabricated using the one-step spin-coating method, and corresponding fabrication procedures are described in detail in the "Experimental Section" in the "Supporting Information." The crystalline structure of the resulting films with different x values was investigated using X-ray diffraction (XRD). As shown in **Figure 1**a, all films show diffraction peaks agree with the typical orthorhombic (B-γ) structure of $CsSnI_3$.[13,24] Moreover, zoomed in on the (202) perovskite plane reveals a peak shift toward higher angles along with the increase of x value, suggesting a shrinkage of the perovskite lattice due to the incorporation of a smaller-radius Br atom. Figure 1b shows the optical absorption spectra of the perovskite films, in which a blueshift of the absorption onset from 980 to 850 nm was observed with the increase of the x value from 0 to 1. Based on the Tauc plots (Figure S1, Supporting Information), it is calculated that the bandgap of the perovskite films increased from 1.26 eV (x 0) to 1.45 eV (x 1), as shown in the inset of Figure 1b. It is worth noting that the bandgap of x 0.4 film is 1.33 eV, which is very close to the ideal bandgap (1.34 eV) of the Shockey–Queisser limit, showing great potential for photovoltaic devices.[25] The normalized steady-state photoluminescence (PL) results are presented in Figure 1c, indicating a blueshift in the emission peak with the increase of x value, which is in well agreement with the absorption spectra. The above results suggest that Br incorporation has no impact on the $CsSnI_{3-x}Br_x$ crystal structure but can largely inf uence their optical bandgap, and thus device photovoltage and efficiency.

Figure 1d–g shows the statistical distribution of the open-circuit voltage (V_{oc}), short current density (J_{sc}), fill factor (FF), and PCE of 20 independent inverted PSCs based on $CsSnI_{3-x}Br_x$ films with different x values. Corresponding photocurrent density–voltage (J–V) curves and photovoltaic parameters of the champion devices are presented in Figure S2 and Table S1 (Supporting Information), respectively. It is obvious that the devices show an increase in V_{oc} and decrease in J_{sc} with increase of the x value, which can be ascribed to the broadening of the bandgap as discussed earlier. In addition, the FF reveals an increment with the increase of x value at first reaching a maximum at x 0.4, but slowly decreased with a further increase of the x value. As a result, the PCE of the devices initially increased and then decreased. The highest PCE of 9.19% derived from $CsSnI_{2.6}Br_{0.4}$-based device suggests that the optimal x value located at 0.4.

Upon achieving the best composition in $CsSnI_{2.6}Br_{0.4}$, we further advance the device performance using commercially available deoxidant DMKO, which was added directly into the perovskite precursor. As illustrated in **Figure 2**a, during the formation of pristine $CsSnI_{2.6}Br_{0.4}$ perovskite film (denoted as control hereafter), abundant Sn(II)-related defects (for example, Sn^{2+} oxidation, Sn_I antisite defects, and halide vacancies or undercoordinated Sn^{2+}) are easily formed due to the ease of oxidation, fast crystal growth rate, and Sn-rich precursor environment.[26] These defects have been reported as formidable factors that deteriorate device performance.[17,27] While, after DMKO addition, the oxidation of Sn^{2+} ions can effectively be suppressed as evidenced by the color change of the precursor

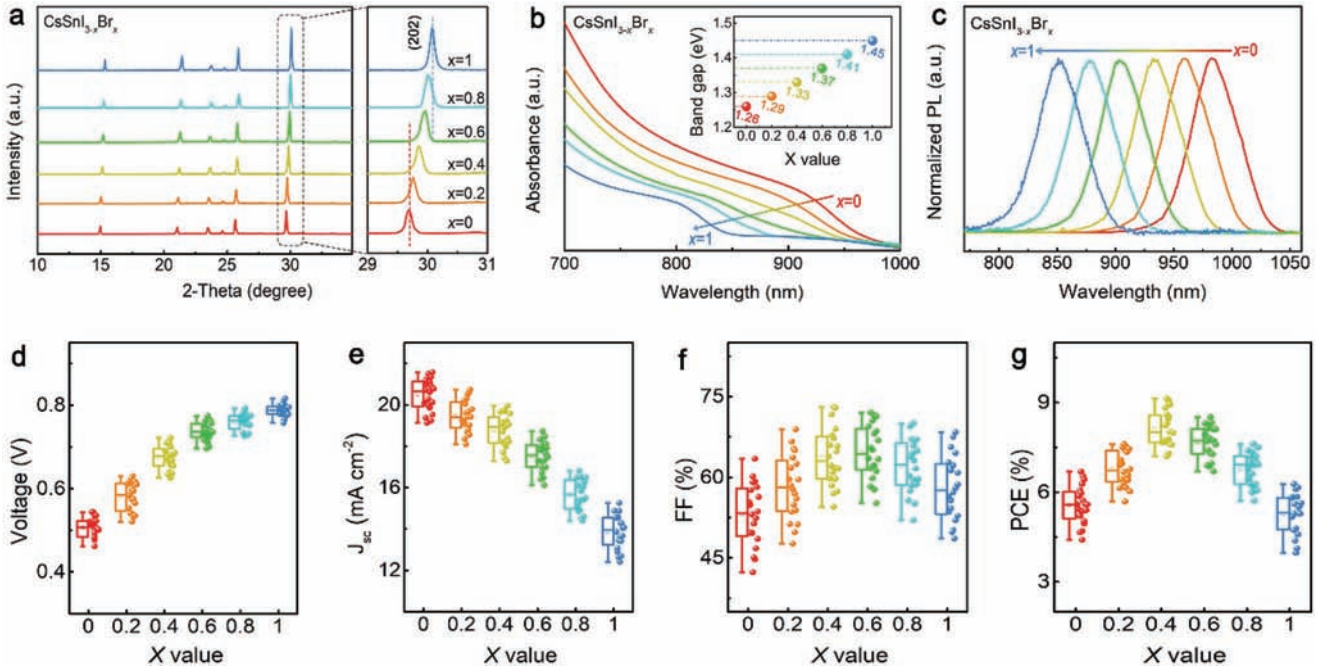

Figure 1. a) XRD patterns of $CsSnI_{3-x}Br_x$ perovskite films with dif erent *x* values. b) Optical absorption spectra and bandgap (inset) of perovskite films. c) Normalized steady-state PL spectra of perovskite films. d–g) Statistical V_{oc}, J_{sc}, FF, and PCE of 20 independent PSCs based on $CsSnI_{3-x}Br_x$ films with dif erent *x* values.

solutions (Figure S3, Supporting Information). The underlying mechanisms can be rationalized as the following equations, in which the DMKO with strong reducibility could neutralize oxygen molecule through Equation (1) and reduce Sn^4 back to Sn^2 through Equation (2). Moreover, we further hypothesized that excess DMKO with the electron-rich oxime group (=NOH) can coordinate with Sn^2 ions, and passivate Sn_I and V_I defects, thus resulting in perovskite films with less structural defects. With the above advantages, it is believed that the multifunctional DMKO additive can significantly enhance the device performance

$$2C_3H_7NO + O_2 \rightarrow 2C_2H_6CO\uparrow + N_2O\uparrow + H_2O \quad (1)$$

$$2C_3H_7NO + Sn^{4+} \rightarrow 2C_2H_6CO\uparrow + Sn^{2+} + N_2\uparrow + 2H^+ \quad (2)$$

To verify the hypothesized mechanisms, a suite of spectroscopy probes were conducted to validate the mitigation of Sn^2 oxidation. Figure 2b–d compares the nuclear magnetic resonance (NMR) spectra of the pure DMKO and DMKO $CsSnI_3$ samples (the $CsSnI_3$ precursor used here was exposed to dry air for 12 h to ensure oxidation of Sn^2 to Sn^4) in deuterated dimethyl sulfoxide-d_6 (DMSO-d_6). As shown in the inset of Figure 2b, pure DMKO solution is colorless and transparent, and oxidized $CsSnI_3$ solution reveals a dark red color due to the high content of Sn^4 .[28] While, after a little amount of DMKO being added, the resulting DMKO $CsSnI_3$ solution appears reddish brown, indicating that the introduction of DMKO contributes to a reduction of Sn^4 concentration. In addition, the ^1H NMR spectra (Figure 2b) reveal that pure DMKO has a resonance peak at 10.16 ppm, which is attributed to the =NOH group. While, for the DMKO $CsSnI_3$ sample, the corresponding resonance peak disappeared, suggesting that the =NOH group in DMKO was expanded through Equation (2). Furthermore, ^{13}C NMR results (Figure 2c) show three characteristic resonance signals at around 152.2, 21.4, and 14.5 ppm, corresponding to C_1, C_2, and C_3 (as denoted in the inset of Figure 2c), respectively. A close inspection of the signals shown in Figure 2d reveals upshift of resonance peaks for the DMKO $CsSnI_3$ sample, further verifying the reaction between DMKO and Sn^4 through Equation (2). The Fourier transform infrared (FTIR) spectroscopy measurements provide the information of chemical interaction between DMKO and $CsSnI_3$, as shown in Figure S4 (Supporting Information). The =NOH stretching vibration of the pure DMKO located at 3278 cm^{-1} is no longer observed when insufficient DMKO (2.5 mg mL^{-1}) was added into $CsSnI_3$ precursor, inferring a complete depletion of =NOH group through Equation (2). However, it should be noted that the corresponding stretching vibration shifted to a lower wavenumber of 3255 cm^{-1} when excess DMKO (5 mg mL^{-1}) was added. Furthermore, X-ray photoelectron spectroscopy (XPS) was conducted to study the chemical compositions and environments of the perovskite films with different DMKO concentrations. As shown in Figure 2e, C 1s core spectra with new binding energy peaks at around 284 and 287.5 eV, which can be indexed to CH_3 and C=N bonds of the DMKO, respectively, are clearly observed when sufficient DMKO was added, demonstrating the existence of DMKO molecule in the final film. This is further supported by the appearance of N characteristic peak in N 1s core spectra shown in Figure S5 (Supporting Information). The O 1s core spectra (Figure 2f) of the films reveal that the proportion of Sn O peak decreases with the increasing DMKO content, which can be ascribed to the deoxidation effect of DMKO through Equation (1). The Sn $3d_{5/2}$ core spectra in

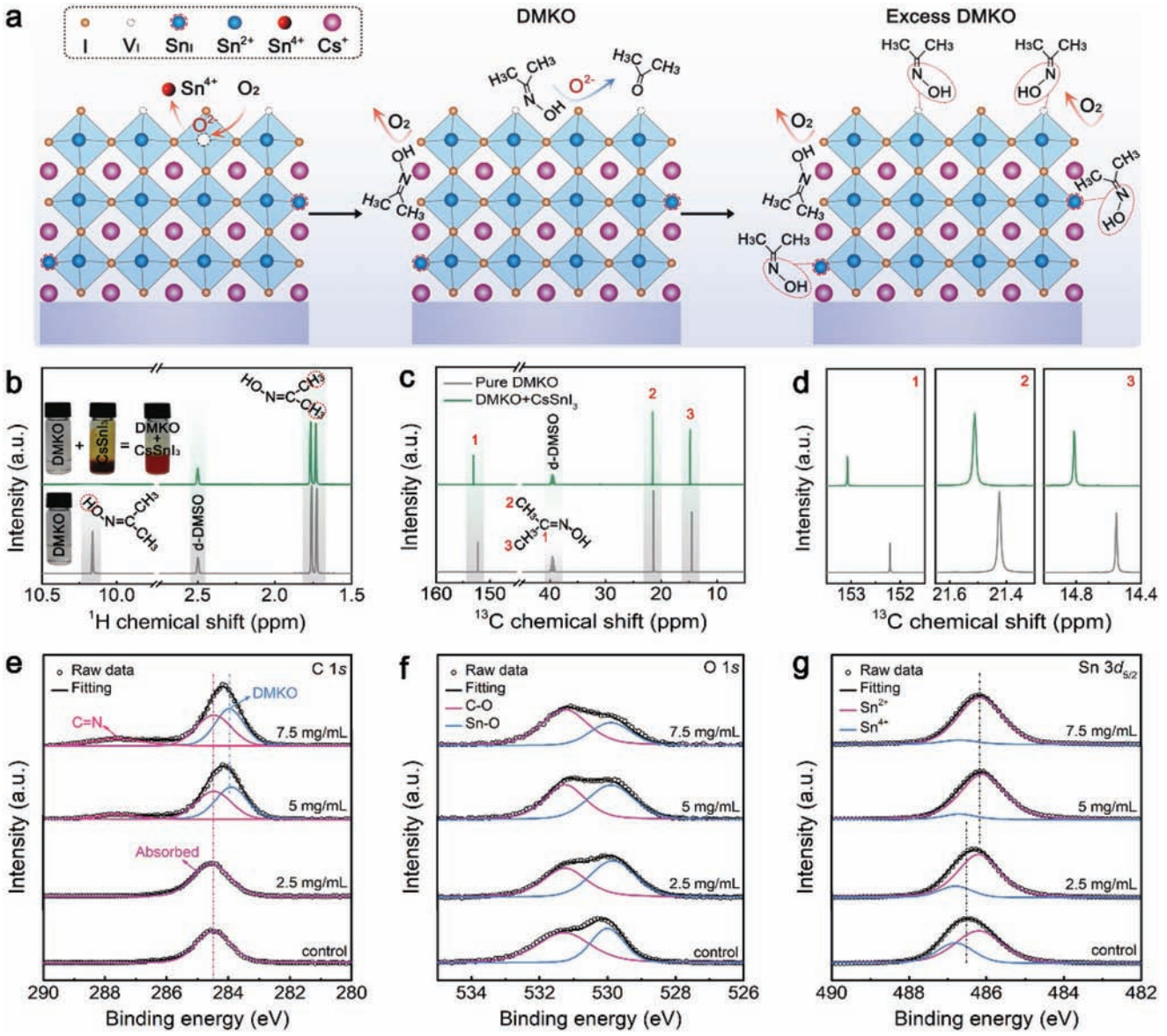

Figure 2. a) Schematic illustration of antioxidation and defect coordination at grain surfaces of $CsSnI_3$ films enabled by DMKO. b) ^1H NMR, c,d) ^{13}C NMR spectra of pure DMKO and DMKO $CsSnI_3$ samples in deuterated DMSO-d_6 solution. e) C 1s, f) O 1s, and g) Sn $3d_{5/2}$ XPS core spectra of perovskite films with dif erent contents of DMKO.

Figure 2g exhibit lower binding energy peak shift from 486.4 to 486.1 eV for control and DMKO samples, further confirming the interaction between DMKO and $CsSnI_3$.[29] More importantly, the proportion of Sn^4 was much reduced after DMKO's introduction, indicating that the oxidation of Sn^2 to Sn^4 has been restrained, in line with discussions related to Figure 2b.[30] These comprehensive, comparative studies of NMR, FTIR, and XPS results have led to the following conclusions: first, DMKO can neutralize a oxygen molecule and reduce Sn^4 back to Sn^2 through Equations (1) and (2) with the expense of =NOH group. Second, insufficient DMKO (2.5 mg mL^{-1}) tends to be totally depleted to neutralize oxygen and reduce Sn^4 . Third, excess DMKO (5 mg mL^{-1}) leads to DMKO residual in the final film and forms coordination with $CsSnI_3$.

To further validate the passivation effect of DMKO on perovskite, DFT calculation including adsorption energy, density of states, and charge density was performed using Vienna ab initio simulation package (VASP). As presented in **Figure 3**a, the ability to obtain/lose electron of the DMKO molecule was quantified by the electrostatic potential surface (EPS) value. The electron-deficit area (positive blue area) is mainly located around H atoms, and the electron-rich area (negative red area) is located around N and O atoms. The ligand of N/O provides a favorable condition for interaction with cations and some specific surface defects, such as Sn_I and V_I defects with extra electrons. Moreover, the interaction between DMKO and perovskite structure was evaluated by carrying out VASP calculations (Figure 3b). Three different Sn(II)-related adsorption locations

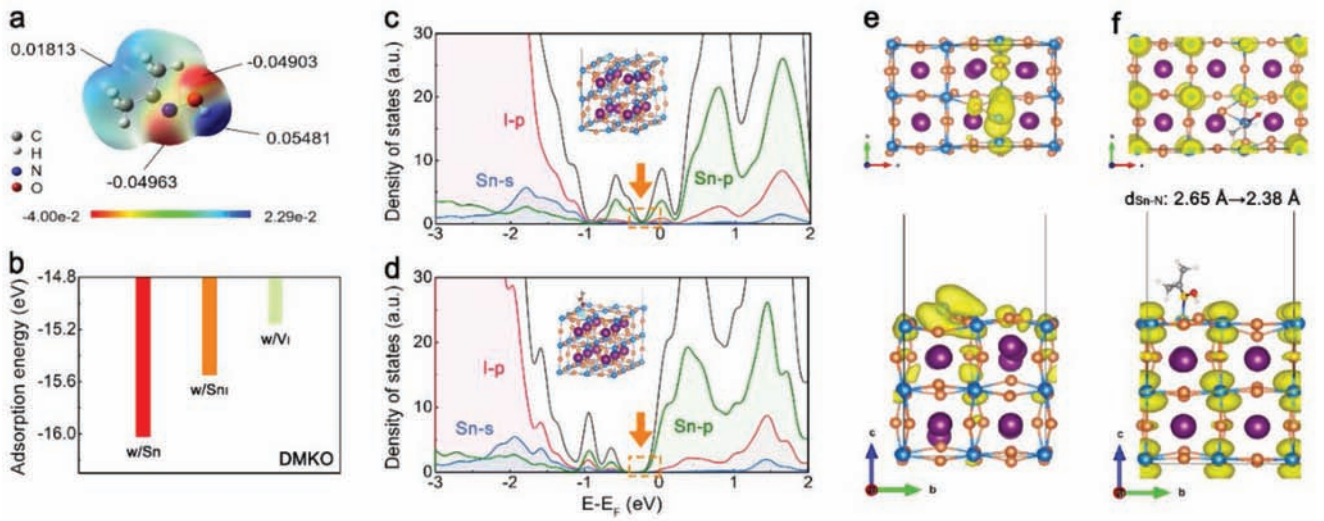

Figure 3. a) Electrostatic potential profile of the DMKO molecule. b) Adsorption energies of DMKO with Sn atoms, and Sn_I and V_I defects. c,d) The density of states and e,f) charge density of perovskite film surface with antisite Sn_I defects and passivated by DMKO.

including Sn atoms, Sn_I and V_I defects were examined, and the adsorption energies are calculated to be –16.02, –15.55, and –15.16 eV, respectively, as summarized in Table S2 (Supporting Information). All adsorption energies of DMKO on the perovskite surface are extremely negative, further suggesting that DMKO can interact with Sn strongly and passivate some specific Sn(II)- and V_I-related detrimental defects. In addition, the density of states and charge density of $CsSnI_3$ surface structures with Sn_I defects and the passivation models with DMKO molecules were calculated and shown in Figure 3c–f, respectively. It is found that the Sn_I defect of the $CsSnI_3$ surface is obviously a trap state indicated by the local charge density around this defect, as depicted in Figure 3e. After passivated by the DMKO molecule, a clean gap appears in the passivation structures as indicated by the inserted orange box in Figure 3d, and the corresponding charge density distributes uniformly at Fermi level shown in Figure 3f. Besides, the structural results show that the bonding length between N of DMKO and Sn decreases from 2.65 to 2.38 Å after geometry optimization, resulting in a more stable perovskite structure. Both experimental analysis and theoretical calculation found that DMKO can interact with $CsSnI_3$ strongly and immobilize the Sn atoms. As a result, the Sn(II)-related defects in perovskite can be efficiently passivated, and the device performance can be significantly improved.

Subsequently, the nanostructure and morphologies of the as-deposited perovskite films with and without the DMKO additive were studied. **Figure 4**a presents the high-resolution transmission electron microscopy (HRTEM) image of perovskite film with 5 mg mL^{-1} DMKO addition (brief y noted as DMKO film hereon). It is noteworthy that clear lattice fringes of perovskite crystal grain can be found, indicating high crystallinity of the film. The *d*-spacing is 0.3 nm, which corresponds to the (202) facet of B-γ $CsSnI_{3-x}Br_x$, as supported by previous studies.[13] Besides, a layer of amorphous DMKO with a thickness of 2.4 nm was clearly identified to cover the $CsSnI_{3-x}Br_x$ crystalline grains, suggesting a grain surface distribution of the residual DMKO. It is believed that this uniformly distributed DMKO can serve as an encapsulation layer, protecting the perovskite film from oxygen, which is critical to the ambient stability of the resulting devices. High-angle annular dark-field (HAADF) energy-dispersive X-ray spectroscopy (EDXS) mapping results of the corresponding perovskite crystal are shown in Figure 4b. It can be observed that all compositional elements, such as Cs, Sn, I, and Br, are distributed homogeneously throughout the perovskite crystal. Additionally, the appearance of N signal further confirmed the existence of DMKO in the final film. The surface morphology of the perovskite films was investigated using scanning electron microscopy (SEM), as shown in Figure 4c,f. Clearly, both control and DMKO films have grown with full coverage of substrates, which are of great importance for high device performance.[31,32] Further, it is noted that control film reveals some cavities and voids in the vicinity of grain boundaries (Figure 4c). Interestingly, with the addition of 5 mg mL^{-1} DMKO, the related defects disappeared, leading to a more compact and uniformed perovskite film (Figure 4f). However, too much content of DMKO (7.5 mg mL^{-1}) leads to poor morphology with obvious DMKO aggregation at the grain boundaries (Figures S6 and S7, Supporting Information), which increases nonradiative recombination, and thereby deteriorates device performance.[33,34] Atomic force microscopy (AFM) images of the films shown in Figure 4d,g suggest that DMKO film has a smaller root mean square (RMS) roughness of 15.9 nm, which is also essential for high device performance.[35,36] The local surface potential of respective films has been studied using Kelvin probe force microscopy (KPFM) in dark. As presented in the insets of Figure 4e,h, the introduction of DMKO contributes to an increase of mean contact potential difference (CPD) value from –35 to 10 mV. It is known that the CPD is a metrics of the potential difference between work function (WF) of sample surface and tip. In this case, the larger CPD value delivers to a smaller work function in DMKO film.

Further, comparative studies on crystalline structure, optical properties, and electronic structures of the resulting films

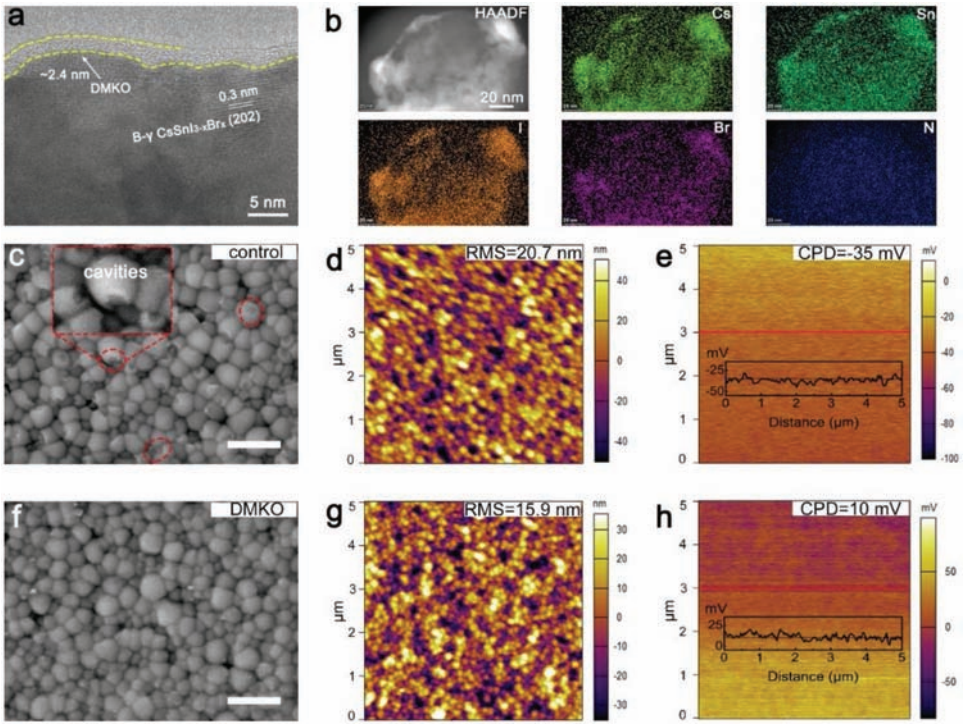

Figure 4. a) TEM image of the as-deposited DMKO film. b) EDXS mapping of key elements in HAADF mode for DMKO perovskite crystal. c,f) SEM images, d,g) AFM images, and e,h) KPFM images of control and DMKO films.

were also conducted. **Figure 5**a shows the XRD patterns of the control and DMKO films. The identical diffraction peaks, which correspond to B-γ $CsSnI_3$ perovskite planes, indicate that DMKO addition did not alter the crystalline structure of perovskite. However, the stronger diffraction peak intensity coupled with smaller full width at half maximum (FWHM, shown in the inset) of (202) perovskite plane suggests that DMKO film has an improved crystallinity.[37,38] The UV–vis absorption (Figure 5b) of the films reveals the same light absorption edge at around 930 nm. While, due to the enhanced crystallinity, the DMKO film exhibits stronger absorption along the visible region.[39] Further, the Urbach energy (E_u) of the films was calculated, and the smaller E_u derived from DMKO film shown in Figure S8 (Supporting Information) further demonstrates a better crystalline film with reduced trap states.[40,41] The corresponding steady-state PL emission peak of the films on quartz glass is located at 932 nm, which is consistent with the UV–vis results. Besides, the much stronger PL intensity suggests that the nonradiative recombination is significantly suppressed within DMKO film. In addition, time-resolved PL (TRPL) measurement was conducted to determine the charge-carrier lifetime of the films, and the results were fitted by a biexponential decay function with detailed parameters summarized in Table S3 (Supporting Information). As shown in Figure 5c, the average carrier lifetime of the control and DMKO films were 8.69 and 15.4 ns, respectively. The prolonged carrier lifetime of the DMKO film is mainly attributed to the improved crystallinity and suppressed nonradiative recombination. The electronic structures of the films were studied using ultraviolet photoelectron spectroscopy (UPS). Figure S9a,b (Supporting Information) shows the obtained secondary electron cutoff (E_{cutoff}) and onset (E_{onset}) energies of the control and DMKO films, respectively. Combining with the optical bandgap (inset of Figure 1b), the positions of conduction band minimum (CBM) and valence band maximum (VBM) of the films were ascertained, and the corresponding parameters are summarized in Table S4 (Supporting Information). As depicted in Figure S9c (Supporting Information), the control film is heavily p-type self-doped, which is attributed to the oxidation of Sn^2 to Sn^4 .[42,43] Interestingly, after DMKO addition, a dedoping process occurred with an upshift of Fermi level (E_F), leading to more intrinsic perovskite film with less trap states and charge recombination.[44] Moreover, it is found that the WF (energy difference between E_{vac} and E_F) of the films decreased from 4.57 to 4.46 eV after DMKO introduction, which agrees well with the KPFM results. This significantly reduced that WF is helpful to charge-carrier extraction and transportation, which are further verified by the faster PL quench and shorter carrier lifetime of the perovskite film fabricated on the hole transport layer (Figure S11, Supporting Information), thus enhancing device performance.

To confirm the effectiveness of DMKO additive on device performance, PSCs with an inverted configuration of indium tin oxide (ITO)/NiO_x/perovskite/[6,6]-Phenyl C_{61} butyric acid methyl ester (PCBM)/zirconium acetylacetonate (ZrAcac)/Ag (Figure 5d) were fabricated. The cross-sectional SEM image (Figure S10, Supporting Information) of the device reveals a uniform stack of functional layers, and the thickness of perovskite layer is about 400 nm. Figure 5e shows the energy level diagram of the devices based on different perovskite films. The well-matched energy level between the perovskite and charge-transport layers (CTL) provides efficient charge extraction and transportation, thus contributing to high device performance.[45]

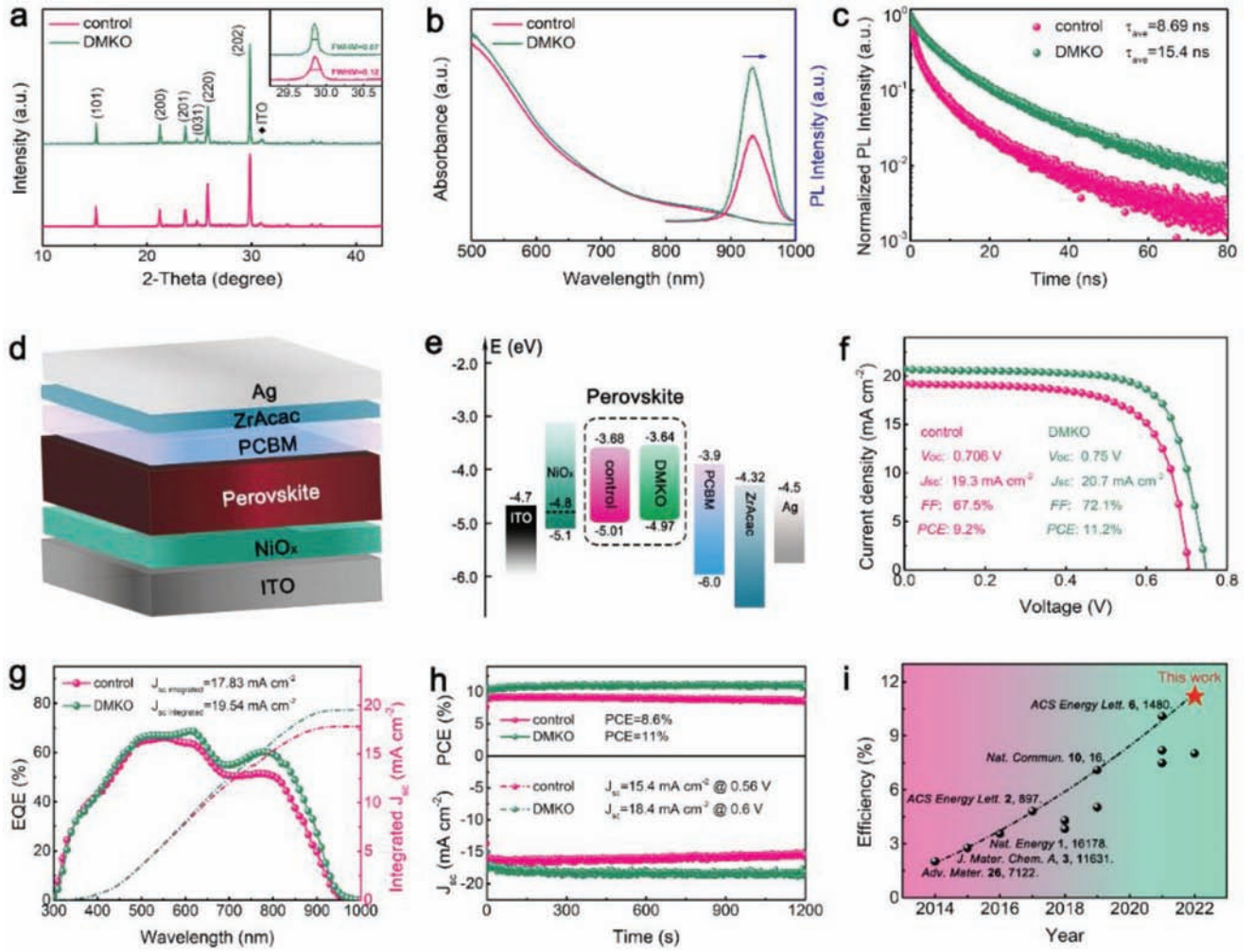

Figure 5. a) XRD patterns, b) UV–vis absorption and steady-state photoluminescence (PL) spectra, and c) time-resolved photoluminescence (TRPL) spectra of control and DMKO films. d) Schematic structure and e) energy level diagram of the devices. f) *J–V* curves, corresponding g) EQE and h) stabilized power outputs of the champion device based on control and DMKO films. i) Efficiency progress of lead-free inorganic PSCs over recent years.

Combining the *J–V* curves of the devices based on perovskite films with different contents of DMKO (Figure S12, Supporting Information) having the photovoltaic parameters summarized in Table S5 (Supporting Information), we can conclude that 5 mg mL^{-1} DMKO addition delivers the optimum device performance. The *J–V* curves of the champion devices based on control and DMKO film are shown in Figure 5f. The DMKO device has an overall enhancement on V_{oc}, J_{sc}, and FF, delivering a PCE of as high as 11.2% (reverse scan) which is much higher than 9.2% for the control device. The significantly improved V_{oc} from 0.706 to 0.75 V is ascribed to the reduced trap density of the perovskite film due to the suppressed self-doping of Sn^2 to Sn^4 and passivated Sn_I and V_I defects after DMKO introduction. However, the J_{sc} enhancement is mainly derived from the decreased work function of the DMKO film, as supported by the KPFM and UPS results. Hysteresis studies based on *H*-index (HI) reveal that DMKO device delivers a smaller HI (9.8%) than that of control (13%), as shown in Figure S13a,b (Supporting Information), which is mainly attributed to a more favorable charge extraction environment in DMKO device.[46] The reproducibility of the devices with DMKO additive is improved due to the mitigated Sn^2 oxidation, as manifested by a narrower PCE distribution (Figure S13c, Supporting Information). Figure 5g presents the external quantum efficiency (EQE) spectra of the devices, where DMKO device shows stronger light response during the visible region, in accordance with the UV–vis absorption. The calculated integrated J_{sc} for the control and DMKO devices are 17.83 and 19.54 mA cm^{-2}, respectively, which are in good agreement with the measured values. To further confirm the reliability of the *J–V* measurements, steady-state power output (SPO) at the maximum power point (MPP) was recorded, as shown in Figure 5h. The PCE values of the control and DMKO device are stabilized at 8.6% and 11% within a 20 min period, respectively, which are close to the values that obtained from the *J–V* curves. Most importantly, it should be noted that the champion PCE obtained here for DMKO device (11.2%) represents the highest efficiency recorded for lead-free inorganic PSCs thus far, as shown in Figure 5i, and with detail

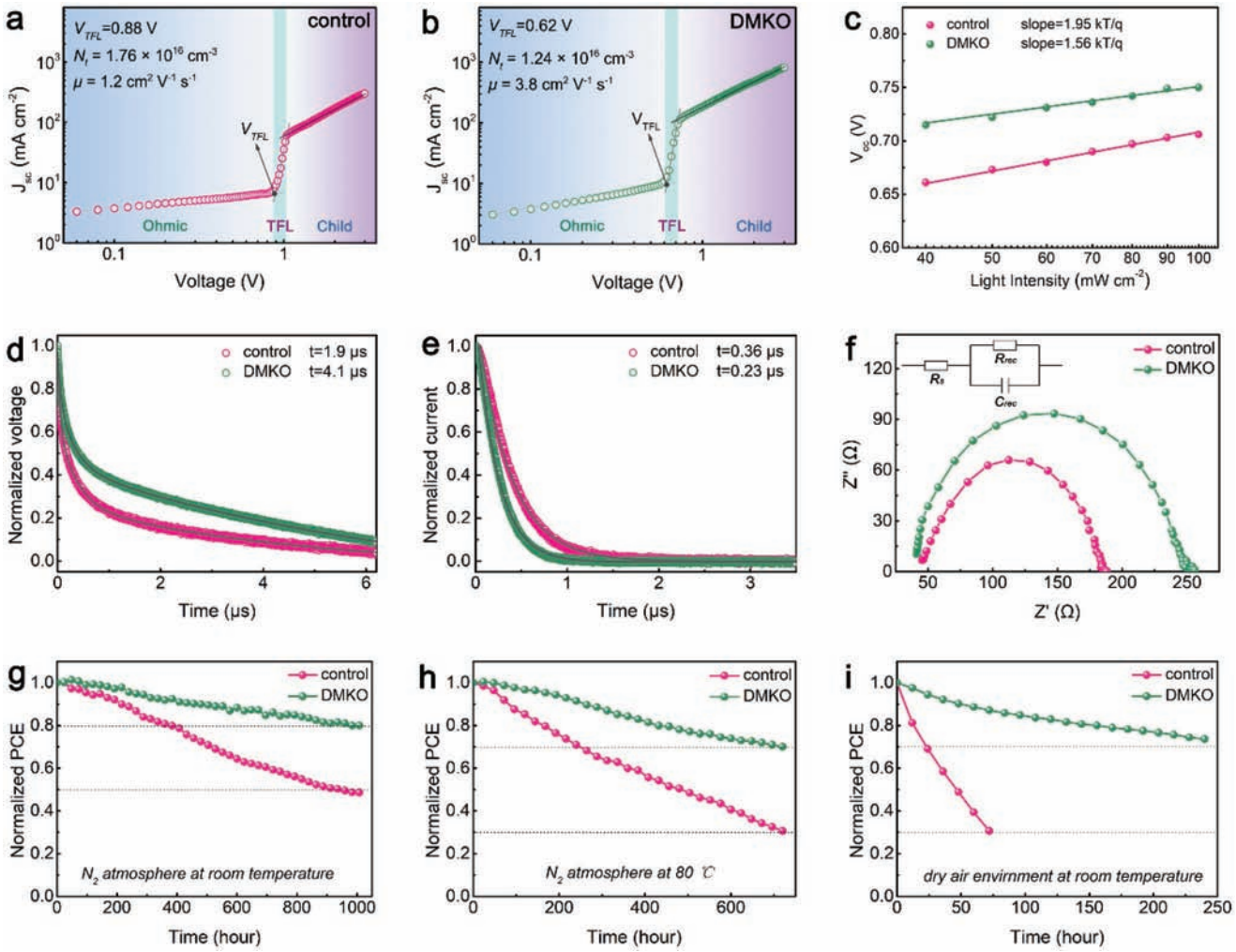

Figure 6. Dark *J–V* curves for the electron-only devices based on a) control and b) DMKO film. c) V_{oc} response under dif erent light intensities. d) TPV and e) TPC results for devices based on control and DMKO films. f) Nyquist plots and equivalent circuit for the dif erent devices. Stability measurements of the un-encapsulated control and DMKO devices under g) glovebox at room temperature, h) glovebox at 80 C, and i) dry air at room temperature.

parameters summarized in Table S6 (Supporting Information). Such an exciting PCE suggests that DMKO is an attractive multifunctional additive for highly performed Sn-based PSCs.

To better understand the significant enhancement of device efficiency, charge dynamic properties of the devices were studied. Space-charge-limited current (SCLC) technique was adopted to quantitatively evaluate the defect density of perovskite films.[47] **Figure 6**a,b shows the dark *J–V* curves of electron-only devices with the device structure of ITO/SnO_2/perovskite/PCBM/Ag. Notably, DMKO-film-based device shows a smaller trap-filled limit voltage (V_{TFL}) of 0.62 V than its control film-based counterpart (0.88 V). It is widely regarded that the trap state density (N_t) can be calculated through the following equation

$$N_t = \frac{2V_{TFL}\varepsilon_r\varepsilon_0}{eL^2} \tag{3}$$

where ε_r is the relative dielectric constant of perovskite, which is 29,[13] ε_0 is the vacuum permittivity, e is the elementary charge, and L is the thickness of the perovskite film, which is 400 nm according to Figure S10 (Supporting Information). Accordingly, the calculated defect density values of control and DMKO films are 1.76 10^{16} and 1.24 10^{16} cm^{-3}, respectively. This reduced defect density of DMKO film is associated with the mitigated Sn^2 oxidation and passivated Sn_I and V_I defects, as discussed earlier. Besides, the electron mobility of the films was estimated using the Mott–Gurney equation as follows

$$\mu = \frac{8J_D L^3}{9\varepsilon_r\varepsilon_0 V^2} \tag{4}$$

where J_D and V are the current density and voltage at the SCLC region, respectively.[48] It is noted that DMKO addition leads to an increase of the electron mobility from 1.2 to 3.8 cm^2 V^{-1} S^{-1}, which is ascribed to the improved crystallinity. In addition, the device response under different light intensities (I) was recorded. As shown in Figure 6c, DMKO device exhibits a smaller V_{oc} versus I slope of 1.56 kT/q than that of control device (1.95 kT/q). It has been reported that the deviation of the slope from unity kT/q indicates the trap-assisted recombination

in PSCs.[34] In this case, the smaller slope suggests that the trap-assisted recombination within DMKO device was substantially reduced, which is responsible for the significant enhancement of V_{oc}. On the other hand, a more ideal α value (0.94) derived from the DMKO device (Figure S14, Supporting Information) suggests that the decreased work function contributes to a higher charge extraction efficiency.[18] Further, transient photovoltage (TPV) and transient photocurrent (TPC) measurements were conducted to better realize the charge recombination and extraction kinetics. The TPV measurements (Figure 6d) reveal that the control device demonstrates a much faster charge recombination decay time (1.9 s) than that of the DMKO device (4.1 s), suggesting a severe charge recombination in control device.[49] Figure 6e shows the TPC results of the devices, where the charge extraction time is decreased from 0.36 to 0.23 s after DMKO addition, indicating an enhanced charge extraction efficiency, which is responsible for the higher J_{sc}.[50] In addition, electrochemical impedance spectroscopy (EIS) measurement is performed to study the interfacial charge transfer and recombination of the devices. Corresponding Nyquist plots were obtained under a bias of 0.5 V in the frequency range from 1 MHz to 1000 Hz under dark conditions at room temperature (Figure 6f). The addition of DMKO contributes to a larger semicircle, which corresponds to a larger recombination resistance (R_{rec}), suggesting that the charge recombination process is effectively suppressed within the device.[51] Overall, the reduced defect density, improved electron mobility coupled with suppressed charge recombination, and enhanced charge extraction efficiency are seen as the main reasons for the significant improvement of photovoltaic performance in the DMKO device.

Besides the device efficiency, the stability issue of Sn-based PSCs is another critical concern for their potential in practical application. To demonstrate the positive effects of the multifunctional DMKO additive on device stability, PCE decay of the un-encapsulated devices under different conditions was recorded. As presented in Figure 6g, the un-encapsulated control device maintains merely around half of its initial PCE after being stored under nitrogen atmosphere at room temperature for 1000 h, while the DMKO device retains over 80% of its original PCE value under the same condition. For the devices stored under nitrogen atmosphere at 80 C, the PCE of the control device remarkably decreased to 30.7% of its original value after 720 h of storage. By contrast, the DMKO device has a much better thermal stability with 70% of its initial PCE maintained (Figure 6h). Furthermore, the un-encapsulated devices were stored under a more severe condition of dry air at room temperature to evaluate their ambient environment stability. As shown in Figure 6i, the PCE of control device quickly drops to 30% of its initial value after 72 h of storage, while the DMKO device maintained 87.1% of its original PCE during the same storage period and retained over 73% of its initial PCE after 240 h of storage. These results suggest that the DMKO additive not only enhances device efficiency but also improves device's long-term thermal as well as ambient stability. The mechanisms behind this much-improved stability can be attributed to the following: first, high-quality DMKO film with less structural defects.[52] Second, the interaction between oxime group and perovskite can inhibit ion migration during heating. Third, DMKO with the reducing oxime functional group decorated at the grain surface leads to encapsulation of the perovskite and restrains oxygen ingress, thus suppressing film degradation under ambient environment.

3. Conclusion

In conclusion, we have demonstrated fabrication of highly efficient and stable lead-free inorganic $CsSnI_{3-x}Br_x$ perovskite solar cells with an optimal I/Br ratio at x 0.4 by using DMKO as the multifunctional additive. Through comprehensive experimental and theoretical studies, we found that the electron-rich oxime group (=NOH) in DMKO not only neutralizes oxidation and reduction of Sn^4 back to Sn^2, but also interacts with Sn^2 ions and passivates Sn_I and V_I defects, resulting in films with high crystallinity, low defect density, and superior charge dynamic properties. Consequently, optimum DMKO concentration leads to a champion PCE of as high as 11.2%, which represents the highest reported efficiency for lead-free all-inorganic PSCs thus far. Moreover, significantly enhanced long-term, thermal, as well as ambient stability of the devices was demonstrated due to the mitigated Sn^2 oxidation, inhibited ions' migration, and restrained oxygen ingress. These results suggest the effectiveness of the multifunctional DMKO as an attractive additive for the realization of highly efficient and stable lead-free inorganic PSCs.

Supporting Information

Supporting Information is available from the Wiley Online Library or from the author.

Acknowledgements

W.Z. and Y.C. contributed equally to this work. The authors thank the National Key Research and Development Program of China (Program No. 2018YFB0704100), the Leading Talents of Guangdong Province program (Program No. 2016LJ06N507), the Shenzhen Basic Research Fund (Grant No. JCYJ20190809144215761), and the National Nature Science Foundation of China (Grant No. 11804117).

Conf ict of Interest

The authors declare no conf ict of interest.

Data Availability Statement

The data that support the findings of this study are available from the corresponding author upon reasonable request.

Keywords

lead free, multifunctional additives, organic free, perovskite solar cells, record efficiency

Received: July 22, 2022
Revised: August 24, 2022
Published online: September 20, 2022

[1] National Renewable Energy Laboratory (NREL), Research Cell Efficiency Records, https://www.nrel.gov/pv/cell-efficiency.html (accessed: January 2022).
[2] J. Zhang, G. Hodes, Z. Jin, S. Liu, *Angew. Chem., Int. Ed.* **2019**, 58, 15596.
[3] W. Zhang, J. Xiong, J. Li, W. A. Daoud, *Small* **2020**, *16*, 2001535.
[4] M. Wang, W. Wang, B. Ma, W. Shen, L. Liu, K. Cao, S. Chen, W. Huang, *Nano-Micro Lett.* **2021**, *13*, 62.
[5] W. Ke, M. G. Kanatzidis, *Nat. Commun.* **2019**, *10*, 965.
[6] T. Miyasaka, A. Kulkarni, G. M. Kim, S. Oz, A. K. Jena, *Adv. Energy Mater.* **2020**, *10*, 1902500.
[7] Q. Tai, K. C. Tang, F. Yan, *Energy Environ. Sci.* **2019**, *12*, 2375.
[8] J. Cao, F. Yan, *Energy Environ. Sci.* **2021**, *14*, 1286.
[9] W. Shockley, H. J. Queisser, *J. Appl. Phys.* **1961**, 32, 510.
[10] C. Yu, Z. Chen, J. J. Wang, W. Pfenninger, N. Vockic, J. T. Kenney, K. Shum, *J. Appl. Phys.* **2011**, *110*, 063526.
[11] Z. Chen, C. Yu, K. Shum, J. J. Wang, W. Pfenninger, N. Vockic, J. Midgley, J. T. Kenney, *J. Lumin.* **2012**, *132*, 345.
[12] M. H. Kumar, S. Dharani, W. L. Leong, P. P. Boix, R. R. Prabhakar, T. Baikie, C. Shi, H. Ding, R. Ramesh, M. Asta, M. Graetzel, S. G. Mhaisalkar, N. Mathews, *Adv. Mater.* **2014**, *26*, 7122.
[13] T. Ye, X. Wang, K. Wang, S. Ma, D. Yang, Y. Hou, J. Yoon, K. Wang, S. Priya, *ACS Energy Lett.* **2021**, 6, 1480.
[14] G. R. Kumar, H. J. Kim, S. Karupannan, K. Prabakar, *J. Phys. Chem. C* **2017**, *121*, 16447.
[15] B. Li, H. Di, B. Chang, R. Yin, L. Fu, Y. N. Zhang, L. Yin, *Adv. Funct. Mater.* **2021**, 31, 2007447.
[16] W. F. Yang, F. Igbari, Y. H. Lou, Z. K. Wang, L. S. Liao, *Adv. Energy Mater.* **2020**, *10*, 1902584.
[17] X. Meng, Y. Wang, J. Li, X. Liu, X. He, J. Barbaud, T. Wu, T. Noda, X. Yang, L. Han, *Joule* **2020**, 4, 902.
[18] W. Zhang, J. Xiong, J. Li, W. A. Daoud, *Adv. Energy Mater.* **2020**, *10*, 2003585.
[19] M. B. Faheem, B. Khan, C. Feng, M. U. Farooq, F. Raziq, Y. Xiao, Y. Li, *ACS Energy Lett.* **2020**, 5, 290.
[20] J. Tian, Q. Xue, Q. Yao, N. Li, C. J. Brabec, H. L. Yip, *Adv. Energy Mater.* **2020**, *10*, 2000183.
[21] Z. Guo, A. K. Jena, G. M. Kim, T. Miyasaka, *Energy Environ. Sci.* **2022**, *15*, 3171.
[22] Z. Wan, H. Lai, S. Ren, R. He, Y. Jiang, J. Luo, Q. Chen, X. Hao, Y. Wang, J. Zhang, L. Wu, D. Zhao, *J. Energy Chem.* **2021**, 57, 147.
[23] Q. Tai, X. Guo, G. Tang, P. You, T. W. Ng, D. Shen, J. Cao, C. K. Liu, N. Wang, Y. Zhu, C. S. Lee, F. Yan, *Angew. Chem., Int. Ed.* **2019**, 58, 806.
[24] T. Ye, K. Wang, Y. Hou, D. Yang, N. Smith, B. Magill, J. Yoon, R. R. H. H. Mudiyanselage, G. A. Khodaparast, K. Wang, S. Priya, *J. Am. Chem. Soc.* **2021**, 143, 4319.
[25] K. Shum, A. Tsatskina, *Nat. Energy* **2016**, *1*, 16016.
[26] T. Shi, H. S. Zhang, W. Meng, Q. Teng, M. Liu, X. Yang, Y. Yan, H. L. Yip, Y. J. Zhao, *J. Mater. Chem. A* **2017**, 5, 15124.
[27] E. L. Lim, A. Hagfeldt, D. Bi, *Energy Environ. Sci.* **2021**, *14*, 3256.
[28] R. Lin, K. Xiao, Z. Qin, Q. Han, C. Zhang, M. Wei, M. I. Saidaminov, Y. Gao, J. Xu, M. Xiao, A. Li, J. Zhu, E. H. Sargent, H. Tan, *Nat. Energy* **2019**, 4, 864.
[29] K. Xiao, R. Lin, Q. Han, Y. Hou, Z. Qin, H. T. Nguyen, J. Wen, M. Wei, V. Yeddu, M. I. Saidaminov, Y. Gao, X. Luo, Y. Wang, H. Gao, C. Zhang, J. Xu, J. Zhu, E. H. Sargent, H. Tan, *Nat. Energy* **2020**, 5, 870.
[30] Q. Chen, J. Luo, R. He, H. Lai, S. Ren, Y. Jiang, Z. Wan, W. Wang, X. Hao, Y. Wang, J. Zhang, I. Constantinou, C. Wang, L. Wu, F. Fu, D. Zhao, *Adv. Energy Mater.* **2021**, *11*, 2101045.
[31] T. Fujihara, S. Terakawa, T. Matsushima, C. Qin, M. Yahiro, C. Adachi, *J. Mater. Chem. C* **2017**, 5, 1121.
[32] Z. Yang, W. Zhang, S. Wu, H. Zhu, Z. Liu, Z. Liu, Z. Jiang, R. Chen, J. Zhou, Q. Lu, Z. Xiao, L. Shi, H. Chen, L. K. Ono, S. Zhang, Y. Zhang, Y. Qi, L. Han, W. Chen, *Sci. Adv.* **2021**, 7, eabg3749.
[33] G. Seo, D. Lee, S. Heo, M. Seol, Y. Lee, K. Kim, S. H. Kim, J. Lee, D. Lee, J. Lee, D. W. Kwak, D. Lee, H. Y. Cho, J. Park, T. K. Ahn, M. K. Nazeeruddin, *ACS Energy Lett.* **2017**, *2*, 1705.
[34] P. You, G. Tang, J. Cao, D. Shen, T. W. Ng, Z. Hawash, N. Wang, C. K. Liu, W. Lu, Q. Tai, Y. Qi, C. S. Lee, F. Yan, *Light: Sci. Appl.* **2021**, *10*, 68.
[35] S. Wang, L. K. Ono, M. R. Leyden, Y. Kato, S. R. Raga, M. V. Lee, Y. Qi, *J. Mater. Chem. A* **2015**, 3, 14631.
[36] W. Zhang, M. Saliba, D. T. Moore, S. K. Pathak, M. T. Horantner, T. Stergiopoulos, S. D. Stranks, G. E. Eperon, J. A. Alexander-Webber, A. Abate, A. Sadhanala, S. Yao, Y. Chen, R. H. Friend, L. A. Estrof , U. Wiesner, H. J. Snaith, *Nat. Commun.* **2015**, 6, 6142.
[37] W. Zhang, J. Xiong, J. Li, W. A. Daoud, *Sol. RRL* **2020**, 4, 1900370.
[38] X. Jiang, F. Wang, Q. Wei, H. Li, Y. Shang, W. Zhou, C. Wang, P. Cheng, Q. Chen, L. Chen, Z. Ning, *Nat. Commun.* **2020**, *11*, 1245.
[39] Z. Xiao, Q. Dong, C. Bi, Y. Shao, Y. Yuan, J. Huang, *Adv. Mater.* **2014**, *26*, 6503.
[40] Y. Chen, N. Li, L. Wang, L. Li, Z. Xu, H. Jiao, P. Liu, C. Zhu, H. Zai, M. Sun, W. Zou, S. Zhang, G. Xing, X. Liu, J. Wang, D. Li, B. Huang, Q. Chen, H. Zhou, *Nat. Commun.* **2019**, *10*, 1112.
[41] A. Rajagopal, P. W. Liang, C. C. Chueh, Z. Yang, A. K. Y. Jen, *ACS Energy Lett.* **2017**, *2*, 2531.
[42] A. B. Wong, Y. Bekenstein, J. Kang, C. S. Kley, D. Kim, N. A. Gibson, D. Zhang, Y. Yu, S. R. Leone, L. W. Wang, A. P. Alivisatos, P. Yang, *Nano Lett.* **2018**, *18*, 2060.
[43] L. Lanzetta, T. Webb, N. Zibouche, X. Liang, D. Ding, G. Min, R. J. E. Westbrook, B. Gaggio, T. J. Macdonald, M. S. Islam, S. A. Haque, *Nat. Commun.* **2021**, *12*, 2853.
[44] Y. Deng, Z. Ni, A. F. Palmstrom, J. Zhao, S. Xu, C. H. Van Brackle, X. Xiao, K. Zhu, J. Huang, *Joule* **2020**, 4, 1949.
[45] W. Zhang, H. Liu, X. Qi, Y. Yu, Y. Zhou, Y. Xia, J. Cui, Y. Shi, R. Chen, H. L. Wang, *Adv. Sci.* **2022**, 9, 2106054.
[46] Q. Jiang, Z. Chu, P. Wang, X. Yang, H. Liu, Y. Wang, Z. Yin, J. Wu, X. Zhang, J. You, *Adv. Mater.* **2017**, *29*, 1703852.
[47] M. I. Saidaminov, A. L. Abdelhady, B. Murali, E. Alarousu, V. M. Burlakov, W. Peng, I. Dursun, L. Wang, Y. He, G. Maculan, A. Goriely, T. Wu, O. F. Mohammed, O. M. Bakr, *Nat. Commun.* **2015**, 6, 7586.
[48] M. I. Saidaminov, M. A. Haque, J. Almutlaq, S. Sarmah, X. H. Miao, R. Begum, A. A. Zhumekenov, I. Dursun, N. Cho, B. Murali, O. F. Mohammed, T. Wu, O. M. Bakr, *Adv. Opt. Mater.* **2017**, 5, 1600704.
[49] K. Jiang, J. Wang, F. Wu, Q. Xue, Q. Yao, J. Zhang, Y. Chen, G. Zhang, Z. Zhu, H. Yan, L. Zhu, H. L. Yip, *Adv. Mater.* **2020**, 32, 1908011.
[50] X. Lian, H. Wu, L. Zuo, G. Zhou, X. Wen, Y. Zhang, G. Wu, Z. Xie, H. Zhu, H. Chen, *Adv. Funct. Mater.* **2020**, 30, 2004188.
[51] P. Tiwana, P. Docampo, M. B. Johnston, H. J. Snaith, L. M. Herz, *ACS Nano* **2011**, 5, 5158.
[52] X. Zheng, B. Chen, J. Dai, Y. Fang, Y. Bai, Y. Lin, H. Wei, X. C. Zeng, J. Huang, *Nat. Energy* **2017**, *2*, 17102.

